Generation of Accurate, High-Resolution Digital Elevation Models from Ultra-Wideband, Drone-Borne, Repeat-Pass Interferometric SAR

Victor Mustieles-Perez, Sumin Kim, *Member, IEEE*, Julian Kanz, *Graduate Student Member, IEEE*, Christina Bonfert, *Member, IEEE*, Alexander Grathwohl, *Graduate Student Member, IEEE*, Gerhard Krieger, *Fellow, IEEE*, and Michelangelo Villano, *Senior Member, IEEE*

***Abstract*—Synthetic aperture radar (SAR) interferometry (InSAR) is a remote sensing technique that allows the generation of digital elevation models (DEMs) by combining two complex SAR images taken with a certain across-track separation. DEMs are of paramount importance for monitoring the Earth's surface and have traditionally been obtained using space- and airborne SAR systems, which are, however, characterized by stringent bandwidth regulations, constrained revisit times, and costly deployment and operation. Drone-borne InSAR enables cost-effective surveillance of local areas with unprecedented accuracy and resolution through the exploitation of wider bandwidths and has therefore emerged as an attractive complementary system with short deployment times and flexible revisit intervals. This paper shows how to generate accurate, high-resolution DEMs through multiple acquisitions performed by a radar with ultrawide fractional bandwidth onboard a drone. We discuss the impact of the characteristics of the system and the acquisition parameters on the quality of the resulting DEMs. We also present a SAR processing scheme based on the omega-k algorithm, which allows fast processing of the drone-based raw SAR data and still yields comparable quality as back-projection algorithms, and an InSAR algorithm that takes into consideration the wide bandwidth of the system and exploits it to support phase unwrapping using radargrammetry. An experimental demonstration is conducted showing that DEMs with a height accuracy of a decimeter can be obtained at an independent posting of 25 cm × 25 cm. The system presented in this paper enables the generation of very high-quality DEMs with very short temporal baselines and also represents an important step towards the realization of single-pass distributed drone-based InSAR systems in the future.**

***Index Terms*—Synthetic aperture radar (SAR), SAR interferometry, digital elevation model (DEM), wide bandwidth, multi-band, multi-baseline, unmanned aerial vehicle (UAV), drones, radargrammetry, phase unwrapping, omega-k algorithm.**

I. INTRODUCTION

SYNTHETIC aperture radar (SAR) interferometry (InSAR) is a coherent remote sensing technique that exploits the phase difference between two complex SAR images to measure range differences with an accuracy of a fraction of a wavelength [1], [2]. In across-track InSAR, the two SAR images are ideally taken from two parallel tracks, whose separation component orthogonal to the azimuth and slant-range directions is known as the perpendicular baseline. The interferometric phase in across-track InSAR depends on the topographic height of the imaged scene and, therefore, this technique is widely used to obtain accurate digital elevation models (DEMs) [3], [4]. InSAR data, and DEMs in particular, are widely used in numerous commercial and scientific applications to monitor the topography of the Earth's surface and its changes over time. Notable applications include mapping surface elevation and topographic changes in ice sheets and glaciers to estimate changes in their volume and mass, monitoring subsidence and erosion, as well as measuring displaced volume associated with, for instance, landslides or volcanic eruptions [4], [5]. Therefore, InSAR is of paramount importance for monitoring the fast-changing dynamics of the Earth's surface and the interest in obtaining higher quality and more frequent data continues to increase [6], [7].

The quality of the DEMs is usually specified in terms of horizontal resolution, or independent posting, and height accuracy. The independent posting depends on the ground resolution of the SAR images used to form the interferogram and on the multi-looking factor (equivalent number of looks). The height accuracy depends on the interferometric coherence, the multi-looking factor and the height of ambiguity, i.e., the scaling factor between the interferometric phase and the

This paragraph of the first footnote will contain the date on which you submitted your paper for review, which is populated by IEEE. This work was partially funded by the Deutsche Forschungsgemeinschaft (DFG, German Research Foundation) GRK 2680 – Project-ID 437847244. Co-funded by the European Union (ERC, DRITUCS, 101076275). Views and opinions expressed are however those of the authors only and do not necessarily reflect those of the European Union or the European Research Council Executive Agency. Neither the European Union nor the granting authority can be held responsible for them. (Corresponding author: Victor Mustieles-Perez).

Victor Mustieles-Perez and Gerhard Krieger are with the Institute of Microwaves and Photonics (LHFT), Friedrich-Alexander University Erlangen-Nürnberg (FAU), 91058 Erlangen, Germany, and also with the Microwaves and Radar Institute, German Aerospace Center (DLR), 82234 Weßling, Germany (e-mail: victor.mustieles@dlr.de).

Sumin Kim is with the Agency for Defense Development, Daejeon, Korea.

Julian Kanz, Christina Bonfert and Alexander Grathwohl are with the Institute of Microwave Engineering, University of Ulm, 89081 Ulm, Germany.

Michelangelo Villano is with the Microwaves and Radar Institute, German Aerospace Center (DLR), 82234 Weßling, Germany.

Color versions of one or more of the figures in this article are available online at http://ieeexplore.ieee.org

topographic height [2]. Large perpendicular baselines can be used with radars with wide bandwidths because the critical baseline, i.e., the baseline for which the two images are totally decorrelated in case of distributed targets, is larger. The increased baseline length enables smaller heights of ambiguity and thus potentially better height accuracies of the DEMs [8]. However, the interferometric coherence decreases due to the difference in the look angles of the two radar antennas and, therefore, a trade-off between the height of ambiguity and the interferometric coherence has to be reached [4], [9]. The two antennas could be located on the same platform, although high accuracies impose, especially at low frequencies, large baselines, which often require the antennas to be located on separate platforms. In addition, spaceborne systems such as TanDEM-X often require the two platforms to fly in formation and operate in bistatic mode (one platform transmits and both receive), or at least in a pursuit monostatic configuration, i.e., the two platforms acquire data independently with a very short time lag, to avoid temporal decorrelation and obtain high DEM height accuracies [4], [10].

Unmanned aerial vehicles (UAVs) or drones equipped with radars are convenient systems for frequent monitoring of local areas, as they are based on easy-to-deploy and cost-effective platforms. Low-altitude drone-borne SAR systems can be equipped with radars that transmit wide bandwidth signals, allowing very high resolutions to be obtained. In many cases, the fractional bandwidth of the radar, defined as the ratio of the system bandwidth to the center frequency, can be very high and even exceed one [11]. The bandwidth available in space- and airborne SAR systems for Earth observation is, in contrast, strongly limited by the International Telecommunication Union (ITU) regulations. Therefore, drone-based SAR emerges as a complementary system to the classical space- and airborne SAR that can allow for flexible, very frequent and high-resolution monitoring of, e.g., natural dynamic processes in local areas through time series of DEMs with high temporal density. In addition, UAVs represent an attractive technology for demonstrating distributed and multi-static SAR concepts for future spaceborne SAR missions [12].

In recent years, UAV-based radar and SAR systems have been extensively investigated for high resolution sub-surface imaging, e.g., for buried object detection [13], [14]. UAV-based SAR systems for high-resolution SAR imaging have also been recently developed. Angelliaume et al. described the development of ONERA's UAV-SAR platform, which operates with a bandwidth of up to 1200 MHz in X-band [15], and Jeon et al. developed a drone-borne L-band radar system that was shown to produce high-resolution mono- and bistatic SAR images [16]. Furthermore, some UAV-based SAR systems with interferometric capabilities have been reported in the literature. Burr et al. showed that single-pass wideband InSAR data acquired from a UAV flying circular trajectories aids in the detection of buried targets [17]. Kim et al. proposed a UAV-borne multi-channel radar system capable of performing single-pass InSAR measurements in W-band [18], where the two antennas were located on the same platform. Moreira et al., presented a drone-borne single-pass InSAR system in P-band for forest inventory [19]. Preliminary repeat-pass InSAR products were obtained by Yocky and West [20], Frey and Werner [21], Lort et al. [22], and Ruiz-Carregal et al. [23]. The aforementioned repeat-pass UAV-based InSAR systems were used to generate preliminary InSAR products, with resolutions comparable to those of spaceborne systems due to the limited radar bandwidths. In addition to the aforementioned InSAR drone experiments, Wang et al. demonstrated a prototype UAV-borne P-band distributed SAR capable of wideband tomographic measurements in a single pass [24].

InSAR from a space- and airborne platform is a well-established technique. Satellites are able to maintain a very stable trajectory which, combined with a sophisticated payload, ensures the correct processing of the data. Processing data acquired from airborne platforms is more challenging, as the aircraft trajectory is not linear and motion compensation methods are required, which also entail limitations. This is even more critical for low-altitude drone platforms for a number of reasons, including: 1) the deviations of a drone track from a linear trajectory relative to the platform altitude are considerably larger and, in many cases, comparable to the largest interferometric baselines that are usable; 2) topographic height variations are often comparable to the drone flight height, which requires accurate motion compensation; 3) positioning systems onboard a drone are less sophisticated than those of an aircraft and the platform is less stable (e.g., in terms of rapid deviations from the ideal track or variation of attitude angles), which requires experimental assessment. Further challenges stem from the use of ultrawide bandwidths and long synthetic apertures to achieve unprecedented resolutions in both dimensions of the SAR image.

In this article, we show how to generate accurate, high-resolution DEMs through multiple acquisitions performed by a radar with ultrawide fractional bandwidth onboard a drone. The considered system performs repeat-pass InSAR, which nevertheless enables very accurate height measurements if compared to spaceborne or airborne SAR systems due to the short time interval between consecutive acquisitions.

The article is organized as follows. Section II presents the system concept, features, and design constraints with special attention to the drone-borne SAR particularities. Section III discusses the SAR and InSAR data processing, where fast processing options based on the omega-k algorithm are also proposed. Section IV shows an experimental demonstration. Conclusions are drawn in Section V.

II. System Concept and Design Aspects

The proposed concept consists of a drone-based SAR interferometer and its main objective is the generation of a DEM of a local area with high resolution and high height accuracy. The indicative target DEM requirements can be identified as follows:

- Height accuracy (standard deviation): < 20 cm
- Independent posting: in the order of 25 cm × 25 cm
- Coverage: in the order of 1 – 5 km^2

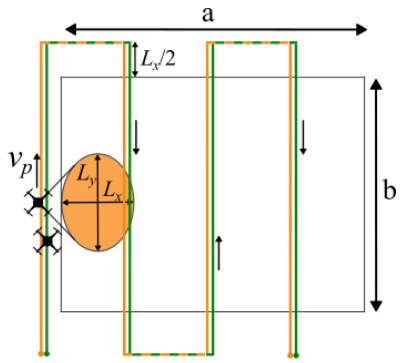

Fig. 1. Example of a drone-borne InSAR acquisition geometry over a rectangular-shaped area of interest.

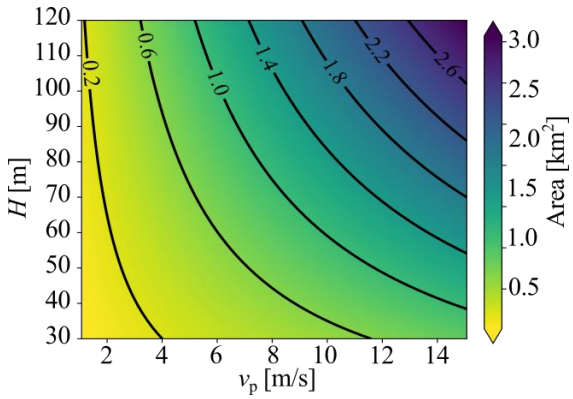

Fig. 2. Estimated imaged area by a drone-borne SAR versus the platform speed and flight altitude, assuming a flight duration of 30 min.

The objective is to achieve the best possible height accuracy for the given independent posting. Both the posting and the height accuracy may be traded off to, for instance, obtain better height accuracies worsening the independent posting. The system design considerations for achieving the above performance using drone-based repeat-pass InSAR are discussed below. The main differences with respect to the design of space- and airborne InSAR systems are highlighted.

A. Coverage Considerations

Coverage is a major constraint of drone-based SAR compared to higher-altitude platforms and is limited primarily by the swath width, acquisition duration, and platform speed.

The swath width is mainly limited by the platform flight altitude and the dependence of the InSAR performance on the incidence angle. To maximize the swath, the maximum possible flight altitude is to be preferred, which for commercial low-altitude drones is currently limited to a maximum of 120 m above ground level by European regulations (higher altitudes up to, e.g., 200 m are allowed, for instance, in China). However, flying at higher altitudes could be possible with the appropriate permissions, in which case the radar transmit power and autonomy may be the limiting factors. The range of incidence angles that can be used is limited by the interferometric performance. Steeper incidence angles result in lower resolution and higher baseline and volume decorrelations, while shallower incidence angles result in lower signal-to-noise ratio (SNR) and larger heights of ambiguity. Therefore, incidence angles between 20˚ and 55˚ are in general preferred for InSAR DEM generation [4]. An antenna beamwidth of about 40˚ in elevation would be required, in order to also account for changes in the platform attitude angle during the acquisition. Considering the aforementioned range of incidence angles from 20° to 55°, the resulting swath width is very close to the platform flight altitude. Given this swath width, a snake-like trajectory could be used to survey a given area, as depicted in Fig. 1. The area of interest is represented as a rectangular shape of dimensions $a \times b$ and L_x and L_y denote the dimensions of the antenna footprint in ground range and along-track directions, respectively. The orange and green lines represent the trajectories of the master and slave drones, respectively.

The acquisition duration is limited by the battery life. Typically, the propulsion power consumption is the limiting factor for the acquisition time, as its consumption is considerably higher than that of the radar system [25]. Typical battery life can range up to about 30 min. As for the platform flight speed, the typical speed of multicopters ranges between 1 and 15 m/s. Therefore, the time T_{acq} to cover a certain area of dimensions $a \times b$ (both assumed to be much larger than the ground swath width W_g and therefore than the height H) can be approximately estimated from the geometry in Fig. 1 and the flight speed and altitude of the platform as follows:

$$T_{acq} \approx \frac{ab}{v_p W_g} \approx \frac{ab}{v_p H}, \tag{1}$$

where v_p denotes the flight speed. It is assumed that there are no border effects, that takeoff and landing times and velocity drop in turns are neglected, and that the swath width is equal to the platform altitude. Fig. 2 shows the estimated surveyed area by a single drone versus H and v_p, assuming a flight duration of 30 min. Considering a single pair of drones flying at an altitude of 120 m with a speed $v_p = 5$ m/s, an area of approximately 1 km^2 can be surveyed in 30 minutes. There is a trade-off between platform speed and acquisition time. On the one hand, one may want T_{acq} to be as short as possible, which requires a high v_p, but on the other hand, one may also limit the maximum v_p to guarantee a minimum SNR, as it will be shown in the following.

B. Geometric Resolution and Number of Looks

The height accuracy of the DEM depends on the interferometric coherence, the height of ambiguity h_{amb}, and the number of looks N_{looks}, which allows improving the height accuracy at the expense of posting degradation [4]. The available number of looks can be approximated as [2]

$$N_{looks} = \frac{\Delta_{rg}}{\delta_{rg}} \cdot \frac{\Delta_{az}}{\delta_{az}}, \tag{2}$$

where Δ_{rg} and Δ_{az} are the required posting in range and azimuth, respectively, and δ_{rg} and δ_{az} are the ground range and azimuth resolutions of each interferometric channel after spectral filtering, respectively.

The azimuth resolution δ_{az} depends on the azimuth angle θ_{az} along which the returns are integrated within the synthetic

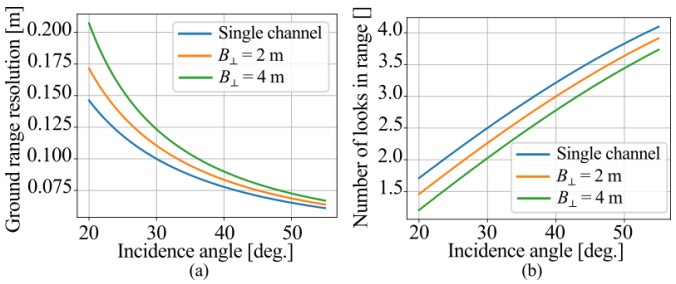

Fig. 3. (a) Ground range resolution of the SAR image and (b) available number of looks in range versus incidence angle for a single interferometric channel and for horizontal baselines of 2 m and 4 m, assuming $H = 120$ m, $B_{rg} = 3$ GHz and $\Delta_{rg} = 25$ cm.

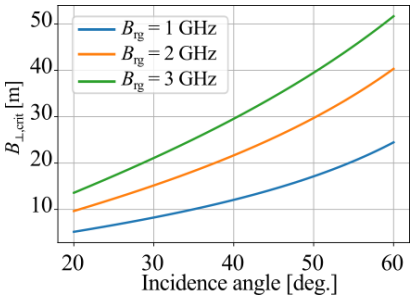

Fig. 4. Critical baseline of the drone-system operating with bandwidths of 1 GHz, 2 GHz, and 3 GHz in X-band, flying at an altitude of 120 m, and assuming flat terrain.

aperture [1]. Wider integration angles yield better azimuth resolutions but are also more difficult to process because the required drone location accuracy increases [11]. In the following, $\delta_{az} = 6$ cm will be assumed, which corresponds to $\theta_{az} = 12^\circ$ in X-band and $\theta_{az} = 43^\circ$ in S-band, resulting in 4.1 looks available in the azimuth dimension. The antenna beamwidth in azimuth should be chosen accordingly, i.e., at least as large as the aforementioned azimuth angle, if a strip-map acquisition is performed.

To calculate the number of independent looks in range, it is assumed that range filtering will be used to optimize the interferometric coherence [4]. Therefore, the common bandwidth may be smaller than that of the individual SAR images, which reduces the available number of looks. δ_{rg} can be approximated in this case as [2]

$$\delta_{rg} \cong \frac{c\cos(\alpha)}{2B_{rg}\sin(\theta_i - \alpha)} \cdot \frac{B_{\perp,crit}}{B_{\perp,crit} - B_\perp}, \tag{3}$$

where B_{rg} is the radar signal bandwidth, c is the speed of light, α is the local slope angle of the terrain, θ_i is the incidence angle, $B_\perp$ is the component of the baseline B perpendicular to the line-of-sight direction, and $B_{\perp,crit}$ is the critical baseline, which can be expressed for the case of wideband repeat-pass InSAR systems as detailed in [26]

$$B_{\perp,crit} \approx \frac{r}{\tan(\theta_i - \beta) + \dfrac{1}{\tan\left(\theta_i \dfrac{B_F}{1 + B_F/2}\right)}}, \tag{4}$$

where $B_F = B_{rg}/f_0$ is the fractional bandwidth of the system, being f_0 the center frequency, r is the range, and β is the angle between the baseline and the horizontal plane in the zero-Doppler plane. Fig. 3 shows in (a) the ground range resolution and in (b) the available number of looks in range versus the incidence angle for the case of the unfiltered and the range-filtered SAR images, assuming horizontal baselines of 2 m and 4 m, $\Delta_{rg} = 25$ cm, $H = 120$ m, an X-band system, and flat terrain. Due to the required range posting of 25 cm, a radar signal bandwidth of 3 GHz is selected for the calculation. The baseline considered is notably below $B_{\perp,crit}$, which is depicted in Fig. 4 together with $B_{\perp,crit}$ for the cases of bandwidths of 1 GHz and 2 GHz, and hence the impact of the baseline in the available number of looks is still small. The criteria for the selection of the baselines to meet the requirement on the height accuracy are discussed below.

C. Selection of Baselines

The standard deviation of the DEM height accuracy σ_h can be approximated for a sufficient number of looks and high values of the interferometric coherence γ_{Tot}, which are usually necessary to meet DEM quality requirements, by its Cramer-Rao lower bound [2]

$$\sigma_h = h_{amb} \cdot \frac{1}{2\pi} \cdot \frac{1}{\gamma_{Tot}} \frac{\sqrt{1 - \gamma_{Tot}^2}}{\sqrt{2N_{looks}}}, \tag{5}$$

where h_{amb} is the height of ambiguity, which can be written as:

$$h_{amb} = \frac{\lambda\, r \sin\theta_i}{2B_\perp}, \tag{6}$$

where λ denotes the wavelength. According to (5) and (6), larger baselines can yield improved DEM height accuracies. However, γ_{Tot} degrades for large baselines, as baseline decorrelation occurs or, if range filtering is used, the number of available looks is reduced, and this also has a negative impact on σ_h. In addition, a small h_{amb} increases the complexity of phase unwrapping, as the variation of the interferometric phase for the same slope becomes proportionally faster [2]. Therefore, baselines should be chosen considering a compromise between these effects. Considering an X-band system, $\theta_i = 45^\circ$, $N_{looks} = 14$ (cf. Section II. B), and $\gamma_{Tot} = 0.6$, which is a reasonable value for the minimum required coherence for drone-borne repeat-pass InSAR acquisitions over surface-like scattering areas with short temporal baselines (cf. Section IV), a maximum $h_{amb} \approx 2.5$ m is allowed to achieve the target height accuracy, which corresponds to $B_\perp \approx 0.9$ m for $H = 120$ m.

Note, that the limited accuracy in the interferometric baseline estimation may cause additional height errors, such as height offsets, in the DEM. They can be reduced by using larger baselines. For instance, a baseline uncertainty of 2 mm in the case of $h_{amb} = 2.5$ m would cause height errors of up to 13 cm, which are reduced to 8 cm for $h_{amb} = 1.5$ m ($B_\perp = 1.5$ m). Therefore, poor baseline estimation accuracy may become the main limiting factor for the achievable DEM height accuracy.

The baselines required to achieve the target σ_h lead to baseline-to-flight altitude ratios in the order of 0.02, a value much higher than that typically used for large-baseline acquisitions in spaceborne (a baseline of 1 km at a satellite altitude of 511 km results in $B/H \approx 0.002$ [27]) and airborne

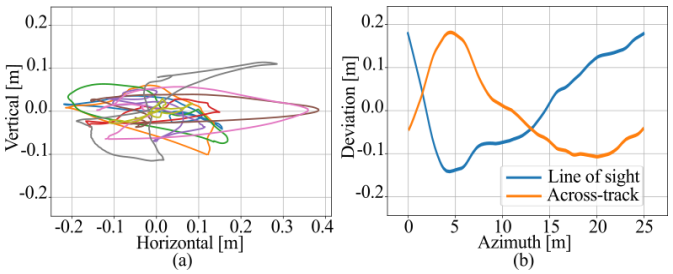

Fig. 5. (a) Deviations from the ideal linear trajectory in the horizontal and vertical coordinates for a set of flown tracks. (b) Measured deviations from a linear trajectory in the line of sight and across-track directions.

(a baseline of 20 m at a nominal flight altitude of 2420 m yields $B_\perp/H \approx 0.008$ [28]) scenarios.

The platform deviations from the ideal straight track have to be considered as well when choosing the baselines. Fig. 5 (a) shows the deviations from the corresponding linear trajectory in the horizontal and vertical coordinates for an exemplary set of tracks. Fig. 5 (b) shows the evolution of the platform deviations from a linear track for a single acquisition both in line of sight and across-track dimensions. The deviations were observed to be larger in the horizontal dimension (up to approximately ± 30 cm) than in the vertical dimension (up to ± 10 cm). Therefore, baselines smaller than approximately 0.5 m may be difficult to achieve in repeat-pass InSAR acquisitions, due to the limited flight accuracy.

D. Noise Equivalent Sigma Zero (NESZ)

In spaceborne SAR, the main factor limiting γ_{Tot} is typically the SNR [4]. In the case of the considered drone-based SAR system, large baselines and platform instabilities are likely to degrade the coherence significantly (cf. Section IV). Therefore, it is reasonable to maintain a high SNR to avoid further decorrelation, e.g., SNR = 13 dB, which results in a coherence value of 0.95 [4]. The SNR can be calculated as the difference in dB between the normalized backscattering coefficient σ_0, which can be taken from Ulaby [29], and the NESZ, whose calculation has some peculiarities compared to the case of space- and airborne SAR. The NESZ can be expressed as follows [4]

$$\mathrm{NESZ} = c_{\mathrm{NESZ}} \cdot \frac{r^3 v_p B_{rg}}{P_{Tx} \lambda^3 \mathrm{PRF}}, \tag{7}$$

where P_{Tx} is the transmitted power, PRF is the pulse repetition frequency, and c_{NESZ} is a factor containing the remaining standard NESZ contributions. This includes the Boltzmann constant, the receiver temperature and noise figure, the system losses, the antenna gains, the speed of light, the pulse duration, and the incidence and slope angles. The σ_0 for soil and rock in VV polarization and X-band with 90th percentile is of the order of -17 dB at $\theta_i = 45^\circ$ [29], hence the NESZ has to be better than -30 dB to obtain an SNR higher than 13 dB. Although the contributions included in c_{NESZ} are predominantly fixed, drone-based SAR allows adjusting several other parameters, which are typically less flexible in space- and airborne SAR systems.

The flight altitude can be varied, although to maximize coverage the maximum possible flight altitude is to be preferred. The flight speed is usually fixed or restricted for satellites and fixed-wing aircraft. For multirotor platforms, however, it is a parameter that can be set with some flexibility in the range of 1 m/s – 15 m/s to ensure a certain SNR level, although it plays also an important role in the coverage achieved. The range of bandwidths that can be used in drone-borne SAR is flexible because the regulation is less restrictive than in spaceborne SAR. However, as mentioned above, the radar signal bandwidth is mainly determined by resolution requirements.

TABLE I
REFERENCE PARAMETERS FOR THE CALCULATION OF NESZ

Parameter	Value	Parameter	Value
Antenna gain (G)	8 dBi	Bandwidth (B_{rg})	3 GHz
Platform height (H)	120 m	Wavelength (λ)	3.3 cm
System losses (L_{sys})	9 dB	Pulse duration (T_p)	1 ms
Receiver temperature (T_{sys})	1000 K	Incidence angle (θ_i)	45°

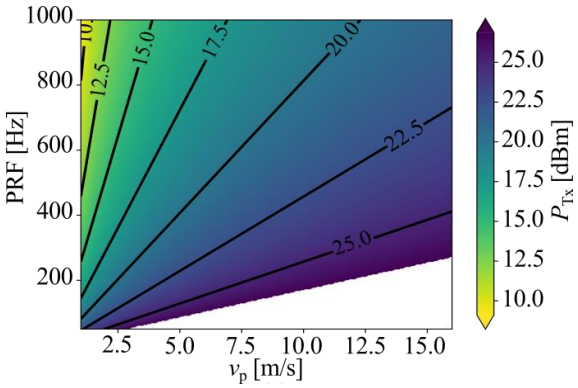

Fig. 6. Required P_{Tx} at X-band to have NESZ $= -30$ dB at $\theta_i = 45^\circ$with respect to the PRF and the platform speed, and assuming the system parameters in Table I.

The PRF is also a parameter that can be widely adjusted, taking into account that it must be larger than the imaged Doppler bandwidth [2]:

$$\mathrm{PRF} \geq \frac{4v_p}{\lambda} \sin\frac{\theta_{az}}{2}. \tag{8}$$

For $v_p = 5$ m/s and $\delta_{az} = 6$ cm, the minimum PRF is about 100 Hz. Unlike spaceborne SAR, drone-borne SAR can operate with a high PRF with no risk of range ambiguities due to the low flight altitudes. For $H = 120$ m and $\theta_i = 60^\circ$, the signal delay is around 1 µs, while the required pulse repetition interval (PRI) is of the order of milliseconds. Therefore, depending on the NESZ requirement, it may be beneficial to use higher PRFs, e.g., up to 1000 Hz. Due to the short-range geometry and the absence of range ambiguities, the maximum PRF is constrained by the pulse duration. Fig. 6 shows the required transmit power P_{Tx} in X-band to have a NESZ $= -30$ dB as a function of v_p and the PRF, assuming the system parameters listed in Table I. The NESZ could hence be adjusted by more than 10 dB without modifications in the transmitted power. The values of P_{Tx} will scale with, e.g., λ or r as indicated by (7). For example, considering flight heights of 60 m and 240 m and keeping constant all other parameters of the radar system, the transmit

power of Fig. 6 will vary respectively by -9 dB and $+9$ dB to keep the same SNR.

A higher P_{Tx} or a higher PRF would also enable a larger coverage for a given acquisition time while maintaining the same DEM quality, since v_p could be increased. Note, that the power required by the propulsion system does not necessarily increase with v_p for multicopters. Hovering is already a power demanding state and the power required by the propellers typically remains almost constant up to a certain speed, which can be about 15 m/s depending on the characteristics of the multicopter [30]. Considering a drone SAR system with parameters $H = 120$ m, $P_{Tx} = 20$ dBm and PRF $= 500$ Hz, the coverage could be increased from 1.2 km^2 to 2.5 km^2 by increasing the transmitted power by 3 dB (see Fig. 2 and Fig. 6). This assumes that the power consumption of the propellers remains approximately constant, which is a reasonable assumption for multicopters [30]. Therefore, unlike in space- and airborne SAR systems, coverage could be increased by allocating more power to the radar system.

III. Data Processing

To process the drone-borne ultrawideband radar data, a processing scheme based on the processors of state-of-the-art airborne InSAR systems such as DLR's F-SAR is used [31]. However, it has to be adapted to take into account the peculiarities and challenges of such a drone system, namely the wide fractional bandwidth and the wide antenna beamwidth, the strong platform instability and the phase unwrapping approach considering the very large interferometric baselines relative to the employed flight altitude. The omega-k (ω-k) algorithm is used for the SAR image focusing, while similar systems employ a SAR processor based on the back-projection algorithm, e.g., [17], [20] – [23]. With today's computing power, the use of back-projection is usually no longer a major concern considering also the smaller swaths of drones compared to spaceborne SAR. However, the use of fast processing is welcome as a step forward to implement the processor onboard and resort to cognitive capabilities in the future. Furthermore, for relatively large areas of, e.g., 1 – 5 km^2, the processing time can be long in view of the very high resolution of the SAR images, which may prevent applications that need the data processed shortly after the flight like disaster monitoring and precision farming.

The overall processing chain is depicted in Fig. 7. It is assumed a frequency-modulated continuous-wave (FMCW) radar, which is commonly used in drone-borne radars, although the signal processing after range compression would be identical when employing pulsed radars [32]. The raw radar data are compressed in range using a fast Fourier transform (FFT) and corrected for the residual video phase (RVP) error, as detailed in [32]. The RVP is an unwanted range-dependent phase term that results after range compression and will cause an interferogram skew if not compensated. It can be neglected for short ranges and small chirp rates, i.e., the pulse bandwidth divided by the pulse duration, but this does typically not apply for drone-borne ultra-wideband SAR. Assuming $B_{rg} = 3$ GHz

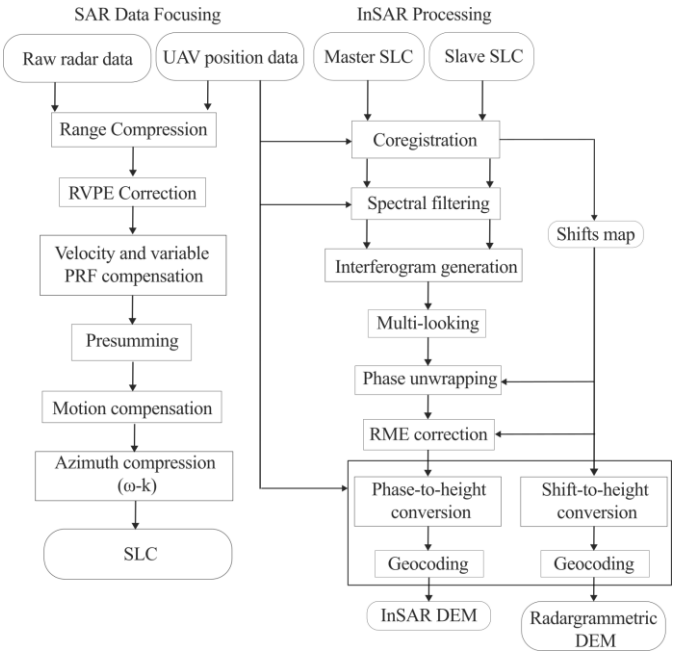

Fig. 7. Flowchart of the SAR and InSAR data processing.

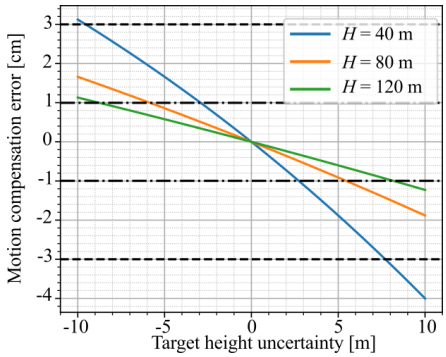

Fig. 8. Error resulting from the calculation of the motion compensation terms due to an uncertainty in the terrain height, assuming an incidence angle of 45° and a platform deviation in the zero Doppler plane of 20 cm both in the horizontal and vertical dimensions. The dashed and dashed-dotted lines indicate the values $\pm\lambda/4$ for center frequencies equal to 2.5 GHz and 7.5 GHz, respectively.

and $T_p = 1$ ms, the residual video phase is about 0.5 rad and 3 rad for ranges of 30 m and 100 m, respectively. Afterwards, the variable platform velocity as well as the variations in the PRF are compensated for by interpolating the radar data to a uniform grid in azimuth and range. The range-compressed data are then presummed to reduce the data volume and speed up the processing. Due to the wide fractional bandwidth, a frequency-dependent low pass presumming filter is required to maintain the annulus sector shape of the SAR signal spectrum and reduce the appearance of non-orthogonal sidelobes. Non-orthogonal sidelobes are notable in wideband wide-beam SAR data, especially when the two-dimensional spectrum of the SAR data is not a complete annulus sector, i.e., spectral content is missing [33], [34].

After presumming, trajectory deviations from a straight line have to be corrected. Precise motion compensation has stringent requirements on the knowledge of the scene topography due to

the short-range geometry of the acquisition. Fig. 8 shows the errors resulting from the calculation of the motion compensation terms as a function of the target height error for different flight heights and in the case of platform deviations in the zero Doppler plane of 20 cm both in the horizontal and vertical dimensions. For a flight height of 40 m, a knowledge of the target height better than 7.5 m and 3.5 m is required for the error to be less than $\lambda/4$ in the cases of center frequencies equal to 2.5 GHz and 7.5 GHz, respectively. The error decreases for higher flight altitudes and the same platform deviation. In the Motion compensation is applied and the data are focused using the omega-k algorithm. Furthermore, processing based on the back-projection algorithm is also applied as a reference processing scheme for comparison. The main output of the SAR processing is a single-look complex (SLC) image.

InSAR processing starts with image coregistration, which is a critical step in InSAR and especially important in our case, considering the very high resolution of SAR imagery. A multi-step coregistration is used [35]. The first step comprises the coregistration using the acquisition geometry and positioning data of the drone. In a second step, the coregistration is refined by means of cross-correlation-based coherence maximization. The size of the cross-correlation patch is progressively adapted in two steps from 1 m × 1 m to approximately 0.4 m × 0.4 m to correctly track topographic variations. The final refinement of the coregistration is achieved using a spectral-based coregistration technique [36]. The outcome of the coregistration stage are, on the one hand, the coregistered SLCs, and, on the other hand, a map of the shifts applied to the SAR data in the azimuth and range dimensions.

The geometric decorrelation is lower in wideband InSAR systems, but is still evident when large baselines are employed. This decorrelation can be avoided at the expense of resolution degradation by filtering the range spectra of the InSAR data pair to a common frequency band in range. The performance of the spectral filtering with wideband signals in the case of large baselines can be notably improved by accounting for the spectral shrinkage along with the spectral shift [26]. In the cases of air- and drone-borne SAR, the incidence angle, and hence the spectral shift, varies strongly along the swath and thus an efficient implementation of the filters for the entire swath is needed. A state-of-the-art implementation valid for narrowband signals was proposed by Reigber in [37], where a single low-pass filter is employed for the entire SAR data after compensating for the spectral shift. This implementation is adapted in this work for use with ultra-wideband signals by also accounting for the spectral shrinkage considerations described in [26]. The first step is to align the spectra of both master I_1 and slave I_2 SAR images, which can be achieved by demodulating the SAR signals using the flat Earth phase term $\phi_{fe}(r)$, given by

$$\phi_{fe}(r) = \frac{4\pi}{\lambda}[R_1(r) - R_2(r)], \tag{9}$$

where $R_1(r)$ and $R_2(r)$ denote the slant-range distances between the master and slave sensors and a pixel located in the coregistered images at range r. If available, the interferometric phase extracted from a reference DEM can also be used to account for topography. Although multiplying I_1 by $\exp[j\phi_{fe}(r)/2]$ and I_2 by $\exp[-j\phi_{fe}(r)/2]$ aligns the ground reflectivity spectra, the common band is still not centered in baseband due to the different spectral shrinkages in the case of ultra-wideband signals. Therefore, an additional correction is applied to account for this effect. The master and slave images whose common ground reflectivity spectra are aligned and centered in baseband, I_1' and I_2', can be calculated as:

$$I_1' = I_1 \cdot \exp[j\phi_{fe}(r)/2] \cdot \exp[-j\phi_{wb}(r)] \tag{10}$$

$$I_2' = I_2 \cdot \exp[-j\phi_{fe}(r)/2] \cdot \exp[-j\phi_{wb}(r)] \tag{11}$$

where $\phi_{wb}(r)$ is a phase correction term that accounts for the range-dependent spectral shrinkage of the spectra and can be computed as

$$\phi_{wb}(r) = \phi(r_0) + 2\pi \int_{r_0}^{r} \Delta f_{wb}(r')dr', \tag{12}$$

where r_0 is the nearest range, $\phi(r_0)$ is an arbitrary phase that can be selected to be zero and $\Delta f_{wb}(r)$ is given by

$$\Delta f_{wb}(r) = \frac{f_{wb,1}(r) + f_{wb,2}(r)}{2}, \tag{13}$$

where $f_{wb,1}(r)$ and $f_{wb,2}(r)$ are the center frequencies of the filters, which can be calculated as detailed in [26]. The second step accounts for the varying bandwidth of the filters along the swath. A range-dependent stretching of the spectra can be achieved by a range-dependent resampling as

$$\Delta_r'(r) = \Delta_r \cdot \frac{\overline{W_f(r)}}{W_f(r)}, \tag{14}$$

where Δ_r is the pixel spacing in range, $\Delta_r'(r)$ is the new non-uniform pixel spacing, $W_f(r)$ is the bandwidth of the filter calculated from the parameters of the master acquisition as detailed in [26], and $\overline{W_f(r)}$ is an average value of $W_f(r)$. After this, a single 2-dimensional low-pass filter with range bandwidth $\overline{W_f(r)}$ at zero Doppler can be applied to the data. The reason for employing a two-dimensional filter is to maintain the annulus sector shape of the SAR data spectra and prevent the appearance of unwanted non-orthogonal sidelobes. The cut-off frequencies of the filter for non-zero Doppler frequencies can be calculated by considering that

$$k_{y,0}^2 = k_y^2 + k_x^2, \tag{15}$$

where $k_{y,0}$ denotes the wavenumber in the range dimension at zero Doppler, and k_x and k_y denote the wavenumber in the azimuth and range dimensions, respectively. After filtering, the inverse of the resampling and phase shifting processing steps have to be performed. When comparing the narrowband and wideband implementations, very small differences in the retrieved coherence values were observed. This result is due to the fact that the spectra of the SAR images were already aligned by the multiplication with the flat Earth phase term and therefore any low-pass filter improves the coherence. However, ignoring the large fractional bandwidth results in an overly strong filter that unnecessarily reduces the image bandwidth, i.e., the bandwidth decreases by about 10-15% for baselines of

the order of 15% of the critical baseline and a fractional bandwidth of 1.2, which corresponds to a reduction of the signal bandwidth by around 300 MHz. Therefore, the proposed implementation optimizes the filtered bandwidth while minimizing the coherence loss due to the baseline.

The interferogram is formed and multi-looked, and the interferometric phase is unwrapped. The map of shifts obtained in the coregistration stage, i.e., the radargrammetric shifts, can be used to support the unwrapping of the interferometric phase, as described in our previous work [26]. Due to the short-range acquisition geometry, the non-linearity in the phase-to-height conversion is stronger than in air- and spaceborne systems. Therefore, it is convenient to directly compare the shifts derived from the interferometric phase and the radargrammetric shifts. The range shifts Δr_{flat} are calculated from the flattened interferometric phase ϕ_{flat}, i.e., the interferometric phase after ground phase removal [31], and are given by

$$\Delta r_{flat} = \frac{\lambda \phi_{flat}}{4\pi}. \quad (16)$$

Considering as well the absolute shifts from the radargrammetric measurement Δr_{ref}, the correct phase cycle is selected according to

$$\Delta r_{unw} = \Delta r_{flat} - \left\lfloor \frac{\Delta r_{ref} - \Delta r_{flat}}{\lambda/2} \right\rceil \lambda/2, \quad (17)$$

where Δr_{unw} represents the corrected range shift obtained from the unwrapped interferometric phase, and $\lfloor \cdot \rceil$ is the operation of rounding to the nearest integer.

InSAR requires ideally straight trajectories along the synthetic aperture, which is a major challenge for airborne systems and especially for drones. In addition, sufficient overlap between the imaged Doppler spectra is required for InSAR. Platform orientation and flight direction are normally correlated in fixed-wing aircrafts. In multicopters, however, this is not the case and the two effects affect the acquired InSAR data differently.

The changes in the flight direction cause phase errors due to residual motion errors (RME) caused by Doppler centroid variation that have to be corrected. Here, the multi-squint approach proposed by Reigber et al. is used, where the time-varying baseline errors are estimated from the azimuth shifts calculated using spectral diversity and using multiple azimuth sub-apertures to improve the estimation in decorrelated areas [38]. Tilts and offsets in the DEMs caused by constant and linear baseline errors are corrected by exploiting data in the overlapping areas between contiguous DEMs, whose height difference is minimized.

The DEM is formed from the corrected shifts obtained from the unwrapped interferometric phase as described in [39]. For the conversion, the moving average of the antenna positions along the synthetic aperture is considered. A DEM is also generated from the radargrammetric shifts. The individual DEMs are then geocoded to East-North-Up (ENU) coordinates and mosaicked using an approach similar to TanDEM-X [40]. The mosaicked DEM is formed from a weighted average of the heights of the individual DEMs. The weights are calculated considering the expected height error of each DEM and the distance to the edge of the DEM, in order to mitigate discontinuities between contiguous DEMs.

TABLE II
REFERENCE PARAMETERS OF THE UAV SAR SYSTEM

Parameter	Value	Parameter	Value
Frequency band 1	1 – 4 GHz	Tx power band 1	15 dBm
Frequency band 2	6 – 9 GHz	Tx power band 2	10 dBm
UAV speed	2 m/s	Duty cycle	0.8
Noise figure	6 dB	Antenna gain	6 dBi
Additional losses	3 dB	Antenna mounting	45°
Pulse repetition frequency	300 Hz	Antenna beamwidth in azimuth	50°
Signal quantization	12 bits	Antenna beamwidth in elevation	60°
Positioning system	RTK-GPS/IMU	Location accuracy	<1 cm

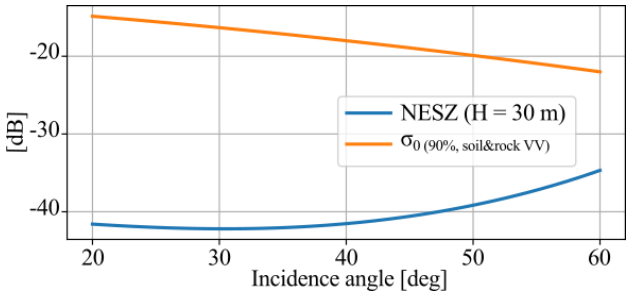

Fig. 9. NESZ and σ_0 used for SNR calculation.

IV. THEORETICAL ASSESSMENT OF THE DEM PERFORMANCE

The expected height performance of the DEMs that will be generated from the experimental data is analyzed in detail in this section. For the analysis, the system parameters in Table II (which are the parameters of the system employed for the demonstration) corresponding to the 6 – 9 GHz frequency band, as well as a flight altitude of 30 m and a horizontal baseline of 0.75 m are considered. The height accuracy of the final DEM depends on the multi-looking factor, the height of ambiguity and the interferometric coherence γ_{Tot} between the two SAR images. The coherence can be estimated as the product of several contributions [4]

$$\gamma_{Tot} = \gamma_{SNR} \cdot \gamma_{Amb} \cdot \gamma_{Quant} \cdot \gamma_{Rg} \cdot \gamma_{Az} \cdot \gamma_{Vol} \cdot \gamma_{Temp}, \quad (18)$$

where the various factors correspond to limited SNR γ_{SNR}, presence of ambiguities γ_{Amb}, signal quantization γ_{Quant}, baseline decorrelation as well as misregistration in range γ_{Rg}, non-overlapping Doppler spectrum as well as misregistration in azimuth γ_{Az}, volume decorrelation γ_{Vol}, and temporal decorrelation γ_{Temp}, respectively. It is assumed that γ_{Quant} is negligible due to the large number of bits used in quantization. γ_{Temp} is also assumed negligible due to sub-hourly temporal baselines and the absence of tall vegetation in most parts of the test field.

The coherence term due to the SNR is computed as [41]

$$\gamma_{SNR} = \frac{1}{\sqrt{(1 + \mathrm{SNR}_1^{-1}) \cdot (1 + \mathrm{SNR}_2^{-1})}}, \quad (19)$$

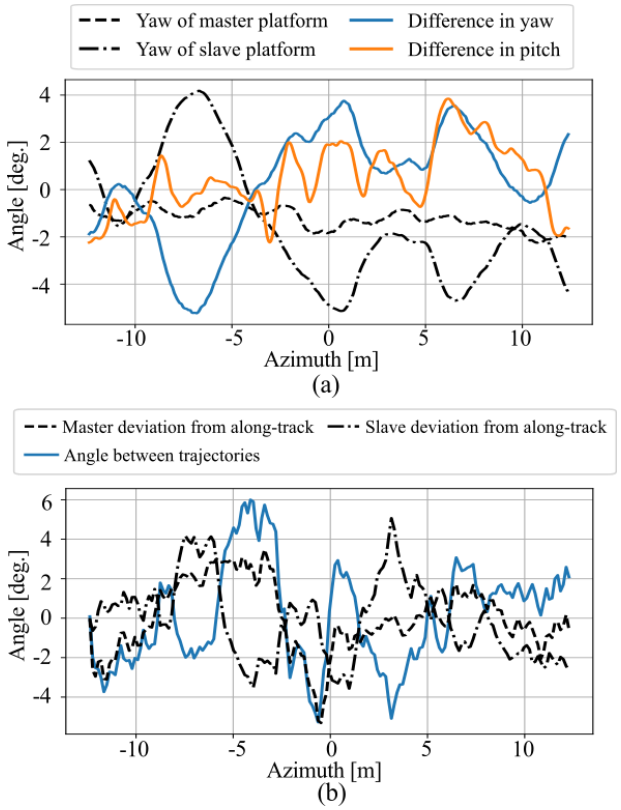

Fig. 10. (a) Yaw and pitch of the master and slave platforms with respect to the along-track direction. (b) Angle of the trajectories followed by the master and slave platforms with respect to the along-track direction.

where $\mathrm{SNR}_{\{1,2\}}$ denotes the SNR of each interferometric channel. The SNR is computed as the difference in dB between the normalized backscattering coefficient σ_0, which in this case is taken from Ulaby [29] for soil and rock in VV polarization with 90th percentile, and the NESZ, calculated using the parameters in Table II. Since large baselines are to be used between the two sensors, the SNR of the two interferometric channels is not assumed to be the same. Fig. 9 shows the calculated NESZ and the σ_0 used to compute the SNR.

The baseline decorrelation is reduced by filtering the signals to a common frequency band [26], and hence γ_{Rg} is only due to misregistration in range. Assuming unweighted processing in the range dimension, γ_{Rg} can be written as $\gamma_{Rg} = \mathrm{sinc}(\pi \cdot \partial r)$, where ∂r denotes the relative shift between the two images in fractions of a resolution cell and $\mathrm{sinc}(x) = \sin(x)/x$ [41]. A coregistration error of 10% results in a coherence coefficient of $\gamma_{Rg} = 0.984$.

The contribution γ_{Az} takes into account misregistration in azimuth as well as a Doppler shift between interferometric channels. In the considered drone case, there is no azimuth displacement between acquisitions and the data are focused to a constant Doppler centroid, which is assumed to be zero. However, the flight direction of the drone, in reality, is constantly changing due to the inherent instability of the platform and, hence, the Doppler centroids vary throughout the data acquisition. From the recorded experimental data (see Section III, Fig. 10), it is reasonable to consider an average difference in the flight direction of the platforms of 2°, while in some cases peaks of 5° are reached. The coherence loss can be then calculated as [41]

$$\gamma_{\mathrm{Az}} = \frac{\int H_1(f) \cdot H_2^*(f) \cdot \exp\left(-j \cdot 2\pi \cdot \frac{\delta_{\mathrm{az}}}{v_p} \cdot f\right) \cdot df}{\sqrt{\int |H_1(f)|^2 \cdot df} \cdot \sqrt{\int |H_2(f)|^2 \cdot df}}, \quad (20)$$

where δ_{az} is the misregistration in azimuth in fractions of a resolution cell, and the azimuth weighting functions $H_1(f)$ and $H_2(f)$ are given by the product of the two-way antenna pattern and the spectral transfer function of the azimuth processing filter, which is assumed constant. The squint angle difference that can be assumed between two drone-borne InSAR acquisitions has been evaluated experimentally. Fig. 10 (a) shows an example of the instantaneous orientation of the master and slave drones considered for an interferometric acquisition. Angular variations within the range -5° to 5° can be observed. Fig. 10 (b) shows the instantaneous orientation of the trajectory of the master and slave drones with respect to the along-track direction for the same exemplary acquisition. A misregistration of 10% is considered, which yields $\gamma_{Az} = 0.853$ for a squint angle difference of 2° between platforms. This value would drop to 0.742 for a squint angle difference of 4°.

The main contribution to γ_{Vol} in the absence of tall vegetation is expected to be ground penetration. It is calculated assuming a vertical exponential reflectivity profile for the ground. The extinction coefficient is calculated from the permittivities measured by Hallikainen for a mid-moisturized clayey soil and for the lowest frequency of the band, which is the worst-case scenario [42].

On the one hand, the range and azimuth ambiguities are negligible due to the low flight altitude and low speed of the drone, respectively. On the other hand, the right-left ambiguity, i.e., opposite-swath ambiguity, needs to be accounted for due to the wide antenna beamwidth in elevation, which is 60° at -3 dB. The measured antenna pattern can be found in [43]. Provided that horizontal baselines are employed in the measurements and the ambiguous signal level is below the main signal level, the ambiguous signal is shifted to a location different to the main signal after focusing and coregistration. Therefore, the ambiguities are assumed to be incoherent with respect to the main signal. Under the previous assumption, γ_{Amb} can then be estimated as

$$\gamma_{Amb} = \frac{1}{1 + \mathrm{ASR}}, \quad (21)$$

where ASR denotes the local ambiguity-to-signal ratio, defined as the ratio of the ambiguous signal to the main signal. If uniform backscattering is considered, the attenuation of the antenna pattern results in signal echoes from the opposite swath between -12 dB and -18 dB with respect to the main signal, resulting in $\gamma_{Amb} = 0.983$ at an incidence angle of 45°.

The estimated overall coherence and the individual contributions are shown in Fig. 11 (a). The DEM height errors are estimated from the interferometric phase errors and the height of ambiguity [4]. The height errors to be expected in the radargrammetric DEM, which is mainly used to support the unwrapping of the interferometric phase, are also calculated

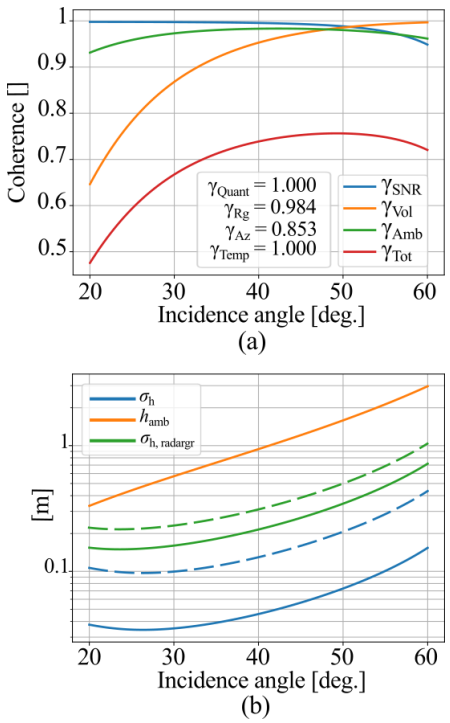

Fig. 11. (a) Summary of all coherence contributions and total estimated coherence. (b) Estimated standard deviation of the height errors of the InSAR (blue) and radargrammetric (green) DEM considering (dashed) and without considering (solid) errors due to the drone position uncertainty, and height of ambiguity of the interferogram (orange).

from the estimated interferometric coherence and the Cramer-Rao lower bound of the standard deviation of the height errors [44]. Fig. 11 (b) shows the estimated height accuracy (standard deviation) of the (solid blue) InSAR σ_h and (solid green) radargrammetric $\sigma_{h,radargr}$ DEMs along with the height of ambiguity of the InSAR DEM h_{amb}. Furthermore, the performance was also analyzed for other baselines considered in the experimental demonstration, i.e., 0.5 m and 1.4 m. The height accuracy in these cases was also below one decimeter.

The uncertainty of the localization system of the drone, which is expected to be in the sub-centimeter range, may cause additional height errors in the DEM. For the same acquisition geometry and assuming a residual positioning error of 2.5 mm, an incidence angle of 45° and a terrain height of 3 m with respect to the reference height, the DEM can exhibit a systematic offset, tilt and height errors due to erroneous h_{amb} estimation up to 1.5 cm, 5 mm/m and 10 cm, respectively [4]. If an additional 10% margin in the interferometric phase errors is considered to account for a possible underestimation of the interferometric coherence, additional height errors can be of around 2 cm. The height errors of the DEM including errors caused by the drone location uncertainty are also shown in Fig. 11 (b) as dashed lines. Therefore, height errors on the order of one decimeter can be expected in the DEM with the system and acquisition configuration considered. As can be seen, the main contribution to the height errors in the DEM is the error caused by the drone position, and hence baseline, uncertainty.

Fig. 12. Photograph of the UAV with the radar system onboard.

Fig. 13. Photograph of the test site including the corner reflectors and the drone flying during an acquisition.

V. Experimental Demonstration

A. Measurement Campaign Description

A repeat-pass InSAR experiment was conducted in June 2023 to demonstrate the performance of the proposed UAV-based InSAR system [45]. The experiment consisted of multiple monostatic SAR acquisitions following linear trajectories with a variety of interferometric baselines and flight altitudes.

The drone-based SAR system is shown in Fig. 12 and consists of the multicopter and a radar system onboard, whose parameters are listed in Table II [11], [17]. The drone is a hexacopter with maximum take-off mass of 12 kg. The localization of the drone for the data processing is measured by a real-time kinematic (RTK) – global positioning system (GPS) and is further enhanced with data from an inertial measurement unit (IMU), allowing position measurements to be obtained with sub-centimeter accuracy [11]. The radar system operates in two different frequency bands, specifically, 1 – 4 GHz and 6 – 9 GHz. It follows the principle of an FMCW radar and is described in detail in [46]. The two frequency bands were acquired together using interleaved radar pulses. Special care must be taken when the radar system includes the frequencies around 2.4 GHz, since this band is normally used to transmit the UAV telemetry signals and interference may occur, resulting in a disturbance added to the useful signal.

The test site is shown in Fig. 13 and consists of an area of

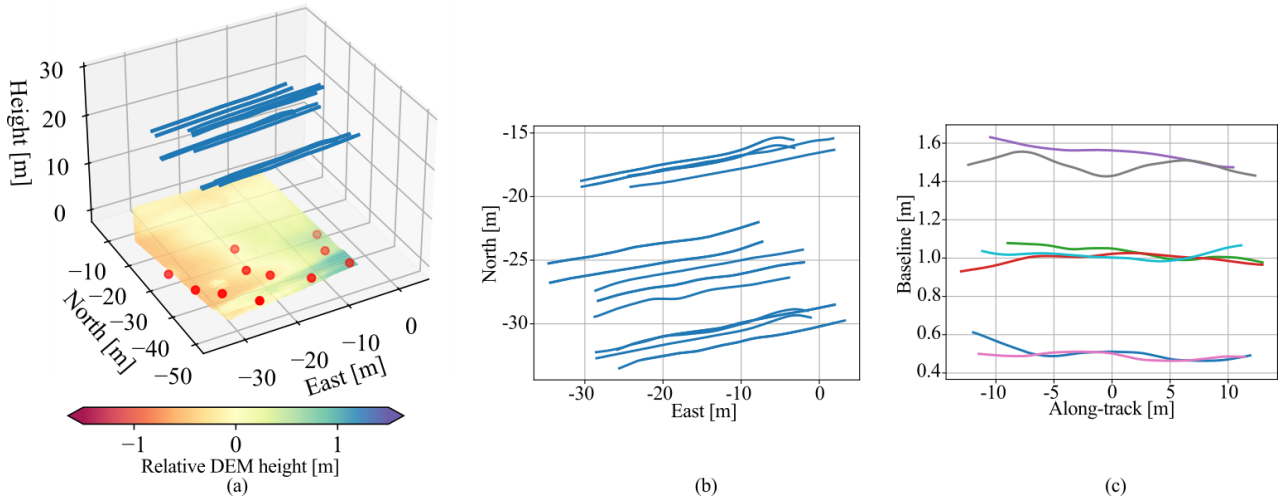

Fig. 14. (a) Scheme of the acquisitions with the flight trajectories represented by blue lines. The DEM measured with the laser scanner is also shown, and the red dots indicate the measured position of the corner reflectors. (b) Projection of the flight trajectories in the horizontal plane. (c) Interferometric baselines in the horizontal plane generated from the flight trajectories depicted in (b).

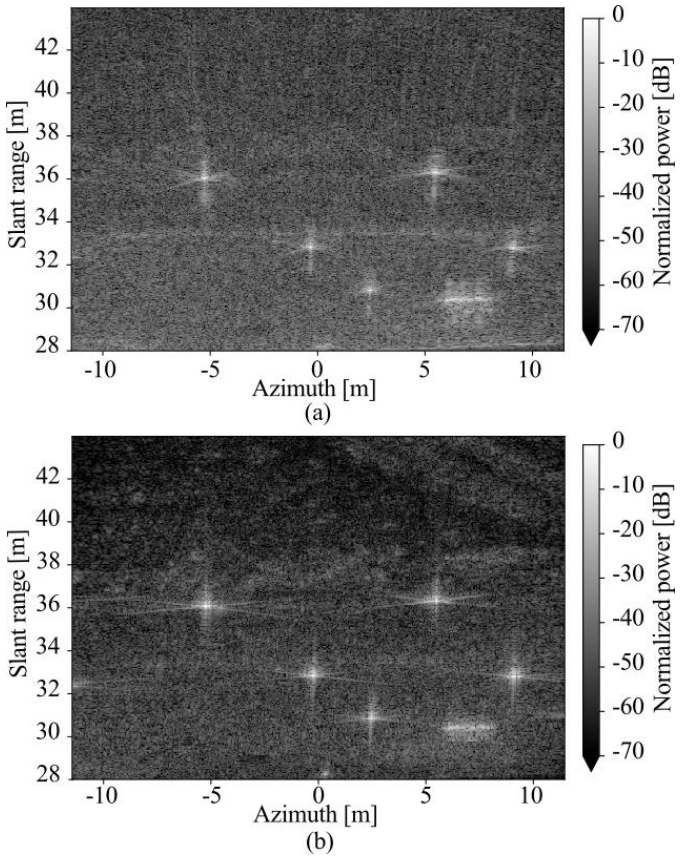

Fig. 15. Focused SAR images of the area containing the corner reflectors acquired in the frequency bands of (a) 1 – 4 GHz and (b) 6 – 9 GHz.

approximately 30 m × 60 m, mostly flat with small topographic undulations and covered by short grass. It also contains a vegetated area with taller grass about 0.5 m high, which is not shown in the photo. Several 55-cm trihedral corner reflectors were placed along the measured area to serve as known references. The position of the corner reflectors was measured to cm accuracy using a differential GPS station. In addition, a ground truth DEM of the test-field was acquired with a three-dimensional laser scanner. The laser scanner is placed on a tripod in the middle of the test field and provides a DEM with cm resolution and height accuracy.

The SAR acquisitions were performed over linear trajectories with nominal flight heights of 20 m and 30 m and horizontal baselines ranging from 0 to 3 m. These baselines correspond approximately to perpendicular baselines up to 15% of $B_{\perp,\mathrm{crit}}$ in the lower frequency band. Higher flight altitudes could not be used in this demonstration due to the limited transmit power of the radar system used for the experiment. Fig. 14 (a) shows a schematic representation of the experimental acquisition with the flown trajectories used to form a DEM of the test field, the DEM measured with the laser scanner and the position of the corner reflectors. Note that, as the radar is left-looking, in some cases the drone flies eastwards, while, in others it flies westwards in order to cover the whole test site. Note also that the drone takeoff, landing and turns have been removed from the representation. Fig. 14 (b) shows the projection of the flight trajectories from Fig. 14 (a) on the horizontal plane. Offsets of up to 1 m in the horizontal plane with respect to the planned trajectories were also observed. Fig. 14 (c) shows the horizontal interferometric baselines generated from the trajectories, which are around the previously planned 0.5 m, 1 m and 1.5 m. The variations of the baseline along the acquisition and within the synthetic aperture are clearly noticeable.

B. Experimental Results

The acquired SAR data are processed following the steps described in Section III. The radar data are presummed, using presumming factors of 9 and 12 for the lower and upper frequency bands, respectively. After motion compensation, the data are focused using the omega-k algorithm. Fig. 15 (a) and Fig. 15 (b) show focused SAR images of the area containing some of the corner reflectors corresponding to the 1 – 4 GHz

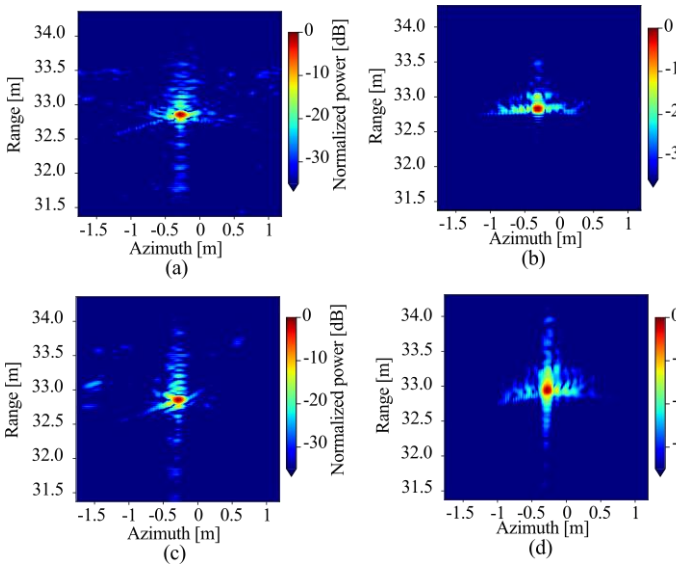

Fig. 16. Omega-k processing results: focused SAR image of a corner reflector in the frequency bands (a) 1 – 4 GHz and (b) 6 – 9 GHz. Back-projection processing results: focused SAR image of a corner reflector in the frequency bands (c) 1 – 4 GHz and (d) 6 – 9 GHz.

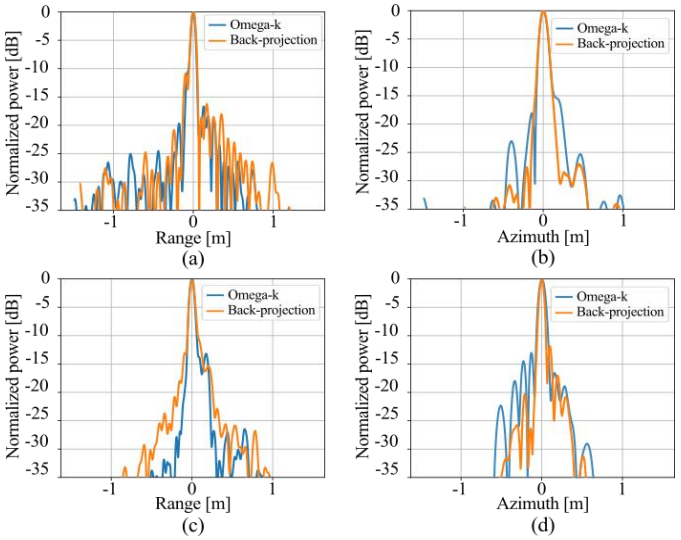

Fig. 17. Comparison of range and azimuth cuts of the SAR images of Fig. 16 obtained with omega-k and back-projection. (a) Range and (b) azimuth cuts of the response of a corner reflector in the case of the 1 – 4 GHz frequency band. (c) Range and (d) azimuth cuts of the response of the corner reflectors in the case of the 6 – 9 GHz frequency band.

and 6 – 9 GHz frequency bands, respectively. The acquisition was performed at an average flight altitude of approximately 27 m. The brighter backscattering at the bottom right of the images corresponds to an artificial metallic target present on the test field. Note the wider sidelobes in range and the non-orthogonal sidelobes in the impulse response function for the case of the 1 – 4 GHz frequency band, which is consistent with the expected response of the point target [33]. The achieved 3-dB resolution is in both frequency bands 6 cm in range and 6 cm azimuth, as the integration time was adjusted to obtain the same azimuth resolution in both frequency bands.

Fig. 16 (a) and Fig. 16 (b) show the SAR images of a corner reflector obtained with the omega-k algorithm for acquisitions in the 1 – 4 GHz frequency band with an integration angle of

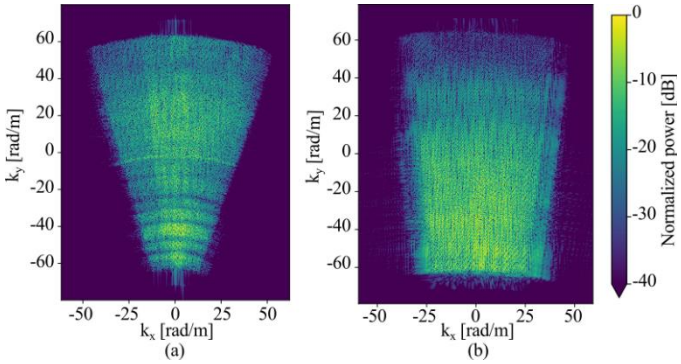

Fig. 18. Two-dimensional spectra of the SAR images for the frequency bands (a) 1 – 4 GHz and (b) 6 – 9 GHz, corresponding to the focused SAR images depicted in Fig. 16 (a) and Fig. 16 (b), respectively.

35° and the 6 – 9 GHz frequency band with an integration angle of 12°, respectively. Fig. 16 (c) and Fig. 16 (d) show the analogous images obtained using the back-projection algorithm for acquisitions in the 1 – 4 GHz frequency band and the 6 – 9 GHz frequency band, respectively.

Fig. 17 (a) shows the range cuts of the responses obtained with the omega-k and back-projection algorithms in the 1 – 4 GHz frequency band, while Fig. 17 (b) shows the azimuth cuts. Fig. 17 (c) depicts the comparison between the range cuts obtained with the omega-k and back-projection algorithms in the 6 – 9 GHz frequency band, while Fig. 17 (d) shows the comparison for the azimuth cuts. The 3-dB resolution achieved in both frequency bands is 6 cm in range and 6 cm in azimuth. Although the SAR data are properly focused with both algorithms, differences are observed, especially considering the side lobes in the image formed in the 6 – 9 GHz frequency band. The main difference between omega-k and back-projection is that motion compensation cannot be ideally applied when using the omega-k algorithm. From the comparison of the impulse response cuts, however, we notice that the achieved resolution is the same and the side lobes are higher in range for back-projection (cf. Fig. 17 (a) and (c)) and higher in azimuth for omega-k (cf. Fig. 17 (b) and (d)).

The spectra of the focused SAR data in Fig. 16 (a) and Fig. 16 (b) are shown in Fig. 18 (a) and Fig. 18 (b), respectively. The annulus sector shape of the spectrum is clearly visible in the SAR data of the 1 – 4 GHz frequency band, since the fractional bandwidth is 1.2 and the integrated azimuth angle is 35°. As mentioned above, maintaining the annulus sector shape is important to reduce the appearance of non-orthogonal sidelobes [33], [34]. The non-uniformities present in the lower half of the spectrum in the 1 – 4 GHz band are due to the interference from the drone telemetry signal, which was mitigated, but a complete elimination was not possible. The shape of the 2-dimensional spectrum of the SAR data in the 6 – 9 GHz frequency band is closer to the typical rectangular shape of spaceborne SARs due to the smaller fractional bandwidth, 0.4, and azimuth integration angle, 12°.

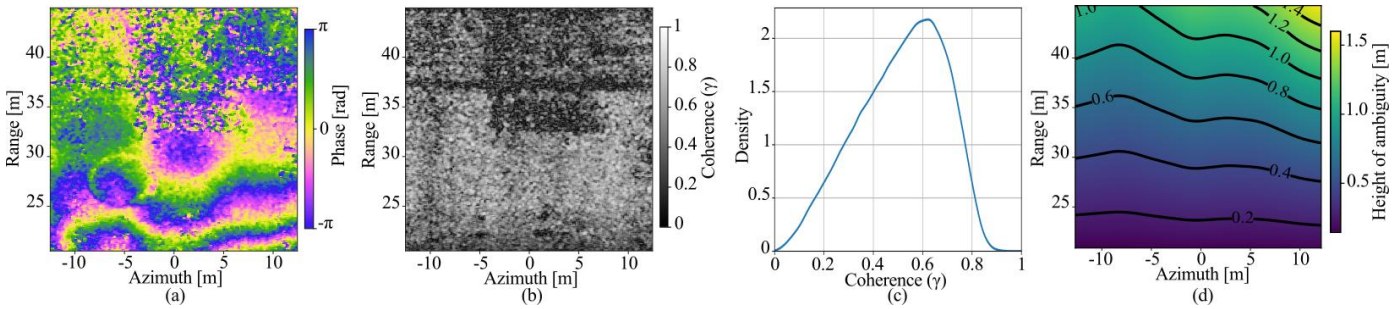

Fig. 19. (a) Multi-looked interferogram (15 looks) in the 6 - 9 GHz frequency band, acquired with a horizontal baseline of 1.5 m at a mean flight altitude of 27 m. (b) Magnitude and (c) histogram of the estimated interferometric coherence. (d) Height of ambiguity of the interferogram.

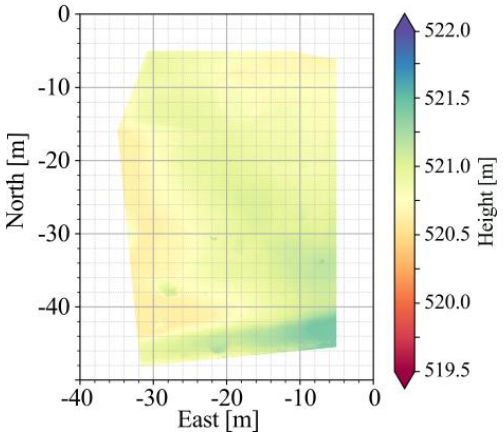

Fig. 20. Ground truth DEM generated from the data acquired over the test field with the 3-D laser scanner.

Fig. 19 (a) shows a multi-looked (15 looks) interferogram of an acquisition with a large baseline (1.5 m) over a nearly-flat area in the 6 – 9 GHz frequency band. The estimated magnitude of the interferometric coherence and its histogram are depicted in Fig. 19 (b) and Fig. 19 (c), respectively. The fringes that appear at the bottom of the interferogram are due to the rapid variation of the height of ambiguity, as shown in Fig. 19 (d), with range. This is a consequence of the short-range geometry. Furthermore, the phase undulations in the azimuth direction are mainly due to the variation of the acquisition baseline, as it can also be deducted from Fig. 19 (d). The decorrelated areas in the interferogram correspond to parts where the vegetation height has a similar magnitude to the height of ambiguity, $h_{\mathrm{amb}} \approx 0.6$ m around slant ranges of 35 m, and to far-range areas where the SNR is lower and the height of ambiguity is larger (slant ranges greater than 40 m correspond to incidence angles greater than 60°). The circular feature visible in the interferogram corresponds to a transition from the short grass of the test field to a bare ground area, which already reflects the height sensitivity of the interferogram.

The individual DEMs are then formed from the interferograms and mosaicked to form a DEM of the entire test site, as it has been described in Section III. The performance of the DEMs obtained from the SAR data is evaluated by comparison with the DEM generated from the laser scanner data, which is used as ground truth. However, it should be noted that the scatterers imaged by the laser scanner and the radar can be different. Therefore, there will always be small discrepancies

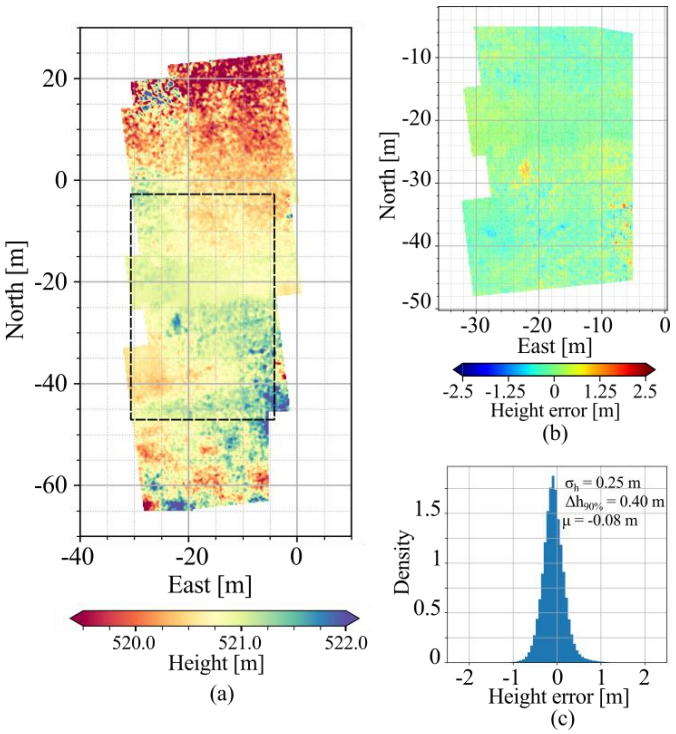

Fig. 21. (a) DEM obtained from the multi-baseline radargrammetric data, (b) map of the height differences between the radargrammetric DEM and the ground truth, and (c) histogram of height differences between the DEMs from radargrammetry and the laser scanner.

between the DEMs generated from the two sensors. In addition, the incidence angle of the laser is very shallow and may also produce small discrepancies between the DEMs formed from the radar and laser data. The absolute height and tilt of the DEM generated from the laser scanner data were calibrated using the corner reflector positions measured with the differential GPS station. Fig. 20 shows the geocoded DEM generated from the point-cloud acquisitions of the laser scanner. A height difference of approximately 1.5 m can be observed between the lowest and highest points of the test field.

To ensure that the InSAR DEM is free of unwrapping errors, the radargrammetric shifts are used as described in the dual-frequency band approach in [26]. A DEM is also generated from the radargrammetric shifts to show the performance difference with respect to InSAR and its capacity to correct phase unwrapping errors. Fig. 21 (a) shows the radargrammetric DEM of the entire test field generated from

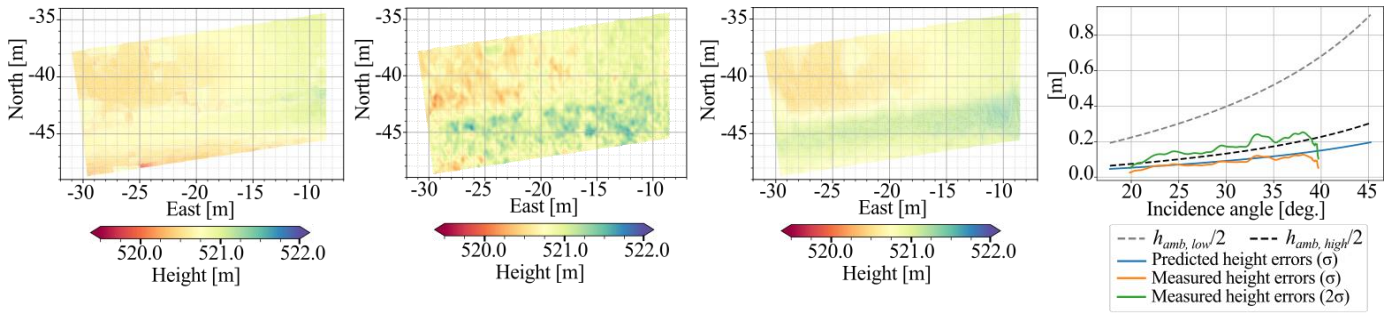

Fig. 22. (a) Geocoded InSAR DEM containing unwrapping errors. Top of the plot corresponds to near range. (b) DEM from radargrammetry used to correct the unwrapping errors. (c) InSAR DEM after phase unwrapping error correction. (d) Height of ambiguity and predicted and measured errors of the radargrammetric DEM with respect to the incidence angle.

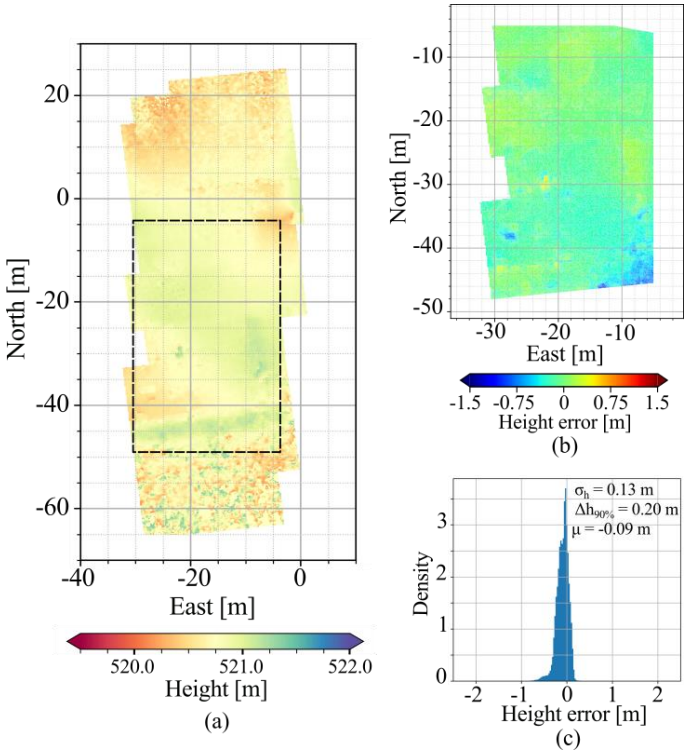

Fig. 23 (a) DEM obtained from the multi-baseline InSAR acquisitions, (b) map of the height differences between the InSAR DEM and the ground truth, and (c) histogram of height differences between the DEMs from InSAR and the laser scanner.

the mosaic of seven partial DEMs. The black rectangle indicates the area for which the ground truth DEM (Fig. 20) is available. Fig. 21 (b) shows the map of height differences between the radargrammetric DEM and the ground truth, and Fig. 21 (c) shows the correspondent histogram of height differences. The standard deviation of the height errors is 25 cm, which needs to be significantly less than $h_{amb}/2$ for an effective correction of phase unwrapping errors. The 90% point-to-point height error $\Delta h_{90\%}$ is 40 cm and the mean of the height errors μ is -8 cm. Based on the predicted performance in Section IV.B., the height accuracy of the DEM from radargrammetry is in good agreement with the predicted values.

Fig. 22 (a) shows a DEM obtained from the InSAR data over a portion of the test field that contains phase unwrapping errors, as can be deducted by comparing it with the ground truth DEM in Fig. 20. Note that, although the difference in terrain elevation is small, there is still a sharp change in height of the order of $1.5 \cdot h_{amb}$ that caused the unwrapping errors. Fig. 22 (b) shows the corresponding radargrammetric DEM that is used to correct the unwrapping errors of the DEM in Fig. 22 (a). Fig. 22 (c) depicts the InSAR DEM after correction of the unwrapping errors, where the better height accuracy compared to the radargrammetric DEM is evident. Fig. 22 (d) shows, with respect to the incidence angle, half of the height of ambiguity for the low $h_{amb,low}/2$ and high frequency bands $h_{amb,high}/2$, the predicted height accuracy (one standard deviation, σ) and the measured height accuracy (one and two standard deviations, σ and $2\,\sigma$, respectively) of the radargrammetric DEM. The height accuracy of the radargrammetric DEM is in good agreement with the predicted value and is notably lower than $h_{amb,low}/2$.

After correcting possible phase unwrapping errors, the InSAR DEM is formed. Fig. 23 (a) shows the DEM over the entire test field resulting from the mosaic of seven partial DEMs obtained from InSAR. The height estimates in the overlapping areas between the DEMs were combined to ensure smooth transitions. The baselines of the acquisitions used yield heights of ambiguity between 0.2 m and 5 m for the individual interferograms. The multi-looking factor is selected to achieve a posting of 25 cm × 25 cm in the DEM. The upper part of the DEM is noisier since all the acquisitions correspond to far range, where the height of ambiguity is considerably larger. The lower part of the DEM has also larger height variations since the terrain contains vegetation approximately 0.5 – 1 m high. The area of the DEM inside the black rectangle is compared to the ground truth generated from the laser scanner acquisitions, the map of height differences is shown in Fig. 23 (b) and the histogram of height errors is shown in Fig. 23 (c). The height errors have a standard deviation of 13 cm, which is on the order of the expected value, according to Section IV. B. Several observations regarding the accuracy of the measured DEM height are worth noting. First, it was observed that the main contribution to the height errors were tilts and offsets of the DEM, most probably caused by residual errors in the drone location and baseline estimation. The standard deviation of the height estimates on the flat part was around 4 cm, which is in

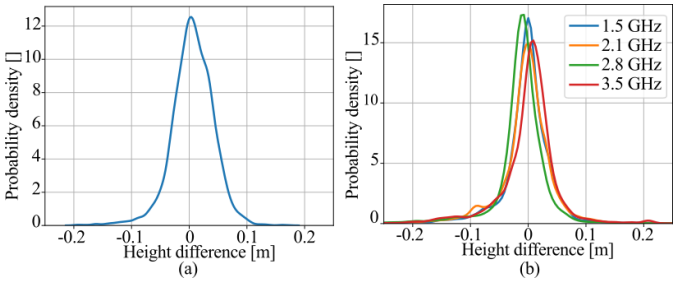

Fig. 24 (a) Height difference between DEMs formed over the flat area covered with short grass from the data acquired in the 1 – 4 GHz and 6 – 9 GHz frequency bands. (b) Height difference between DEMs formed over the flat area covered with short grass from 1-GHz sub-bands with the center frequencies depicted in the legend and the DEM formed from the entire 1 – 4 GHz frequency band.

good agreement with the prediction in Fig. 11 (b). Second, it should be noted that the laser scanner DEM is not a perfect ground truth. Errors in the order of a few centimeters can occur to the very different incidence angles of the laser and the radar and the fact that the radar signals experience some penetration.

Potential height biases in the DEMs due to frequency-dependent ground penetration are an important aspect to be evaluated given the wide frequency range used in the measurements. On the one hand, a significant penetration difference between the 1 – 4 GHz and 6 – 9 GHz frequency bands would affect the performance of the multi-band phase unwrapping using radargrammetry. On the other hand, the signal penetration may be significantly different along the frequency bands used due to the large fractional bandwidths. The possible height bias between the DEMs generated from the data in the two frequency bands is evaluated using a DEM generated from each band over the flat area covered with short grass. To avoid instrument biases, the absolute height of the DEMs is calibrated using the corner reflectors, which resulted in height differences for the corner reflectors of less than 2 cm between frequency bands. The height difference of the 6 – 9 GHz band DEM with respect to the 1 – 4 GHz band DEM is shown in Fig. 24 (a). As it can be appreciated, there is no significant height offset. The penetration difference along the 1 – 4 GHz frequency band is now evaluated. Four sub-bands are generated with bandwidths of 1 GHz and center frequencies of 1.5 GHz, 2.1 GHz, 2.8 GHz, and 3.5 GHz, respectively. To ensure high coherence, the spectral shift and shrinkage are corrected before filtering, as detailed in Section III. Fig. 24 (b) shows the height differences between the DEMs generated from the InSAR data of each sub-band and the DEM generated from the data of the whole band. As in the previous case, very small height offsets are observed.

To illustrate the very high quality of the DEMs that can be generated using InSAR with such a system, let us now consider a small patch of the imaged area containing a transition from short grass to bare ground, as shown in the photograph in Fig. 25 (a), which represents a very subtle topographic change of a few centimeters. Fig. 25 (b) and (c) show the DEM obtained using InSAR acquisitions in the 6 – 9 GHz frequency band with several interferometric baselines and the laser scanner data, respectively. Fig. 25 (d) shows a histogram of the height differences between the DEMs obtained with InSAR and the laser scanner. The achieved standard deviation of the height errors is 7 cm at a posting of 25 cm × 25 cm. Note, that many differences between the two DEMs may be due to different backscattering mechanisms or very different incidence angles, among others.

The quality of the generated DEMs can be compared with results obtained in other experiments over local and predominantly flat areas using state-of-the-art air- and spaceborne InSAR sensors. The combination of multi-baseline InSAR data acquired with TanDEM-X allowed generating DEMs with a height accuracy (standard deviation) and posting of 0.27 m and 6 m × 6 m, respectively [27]. Furthermore, DEMs with a height accuracy (standard deviation) of 5 cm were obtained at a posting of 1 m × 1 m using multi-frequency multi-baseline data acquired with DLR's F-SAR platform [28]. Height accuracies of the same order are achieved with the system described in this paper, while the large bandwidth available on the drone-borne radar allows the resolution to be improved by more than one order of magnitude.

VI. Conclusion and Outlook

A concept to obtain DEMs with unprecedented height accuracy and resolution over local areas with a drone-based ultrawideband InSAR system was proposed and experimentally demonstrated. This is a cost-effective, very rapidly deployable system that can complement classical space- and airborne systems. It will enable the monitoring of very fast changing phenomena thanks to its capacity of generating very accurate

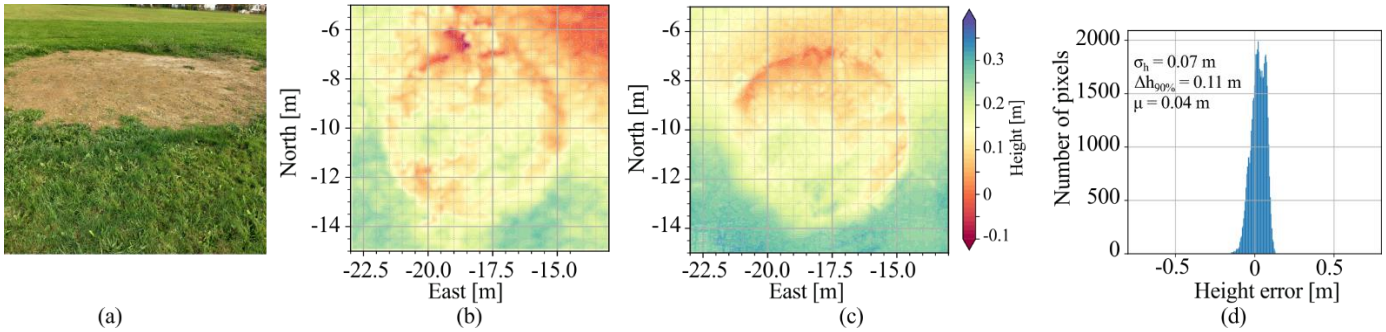

(a)

Fig. 25. (a) Optical image of the transition from grass to bare ground in the test field. DEMs over the same area obtained with (b) InSAR in the 6 – 9 GHz frequency band and (c) the laser scanner. (d) Histogram of height errors between the InSAR and the laser scanner DEMs.

DEMs in a repeat pass using one or multiple drones. It could also be operated as a single-pass system, with proper synchronization between the radars and scaling the baselines by a factor of about two.

The main constraints and challenges of the system design were addressed and the processing chain to obtain the DEMs was presented, in which a fast processing based on the omega-k algorithm was used and radargrammetry was effectively integrated with interferometry to perform phase unwrapping.

The measurement campaign conducted demonstrated obtaining DEMs with a height accuracy of 13 cm (standard deviation) at a posting of 25 cm × 25 cm for the entire test site. This performance implies a resolution improvement of more than one order of magnitude when compared to DEMs obtained with state-of-the-art air- and spaceborne InSAR sensors, which can achieve DEMs with resolutions on the order of one meter mainly due to bandwidth constraints.

While our first demonstration campaign only considered platform altitudes up to 30 m above ground level due to the limitations in the current radar system, drone regulations allow for flight altitudes up to 120 m. This will allow reasonable coverages, e.g., 1 km^2 in 30 minutes with a single pair of drones, which can be scaled up by using multiple platforms. Our results will not only open the door to a new generation of DEMs and height change maps for several local-scale applications, but will also serve for the demonstration and preparation of future wide-band, multi-frequency and/or multi-platform spaceborne SAR missions.

Future research steps include making the system operational in environments with steeper topography and the generation of further interferometric products beyond DEMs, such as elevation change maps or DEM time series for crop monitoring. Improvements in baseline estimation will also continue to be investigated to reduce height errors due to the drone location uncertainty.

ACKNOWLEDGMENT

The authors would like to thank their colleagues P. K. Huggins for his help in understanding frequency-dependent penetration biases in DEMs formed from wideband InSAR data, L. L. Lamberti for supporting the experimental demonstration, and Dr. P. Prats-Iraola and Prof. A. Moreira for sharing their deep knowledge of airborne SAR signal processing and for fruitful discussions and suggestions.

REFERENCES

[1] A. Moreira et al., "A tutorial on synthetic aperture radar," in *IEEE Geoscience and Remote Sensing Magazine*, vol. 1, no. 1, pp. 6-43, March 2013.

[2] R. Bamler and P. Hartl, "Synthetic aperture radar interferometry," Inverse Problems, vol. 14, Art. no. 4, Aug. 1998.

[3] S. N. Madsen, H. A. Zebker and J. Martin, "Topographic mapping using radar interferometry: processing techniques," *IEEE Trans. Geosci. Remote Sens.*, vol. 31, no. 1, pp. 246-256, Jan. 1993, doi: 10.1109/36.210464.

[4] G. Krieger et al., "TanDEM-X: A Satellite Formation for High-Resolution SAR Interferometry," IEEE Trans. Geosci. Remote Sens., vol. 45, Art. no. 11, Nov. 2007.

[5] A. Moreira et al., "Tandem-L: A Highly Innovative Bistatic SAR Mission for Global Observation of Dynamic Processes on the Earth's Surface," in IEEE Geoscience and Remote Sensing Magazine, vol. 3, no. 2, pp. 8-23, June 2015, doi: 10.1109/MGRS.2015.2437353.

[6] J. Mittermayer et al., "MirrorSAR: An HRWS Add-On for Single-Pass Multi-Baseline SAR Interferometry," in IEEE Transactions on Geoscience and Remote Sensing, vol. 60, pp. 1-18, 2022, Art no. 5224018, doi: 10.1109/TGRS.2021.3132384.

[7] A. Reigber et al., "Very-High-Resolution Airborne Synthetic Aperture Radar Imaging: Signal Processing and Applications," in Proceedings of the IEEE, vol. 101, no. 3, pp. 759-783, March 2013, doi: 10.1109/JPROC.2012.2220511.

[8] A. Ferretti et al., "InSAR Principles-Guidelines for SAR Interferometry Processing and Interpretation," ESA Publications, Noordwijk, The Netherlands, Volume 19, 2007.

[9] H. A. Zebker and J. Villasenor, "Decorrelation in interferometric radar echoes," *IEEE* Trans. *Geosci. Remote Sens.*, vol. 30, no. 5, pp. 950-959, Sept. 1992, doi: 10.1109/36.175330.

[10] G. Krieger, I. Hajnsek, K. P. Papathanassiou, M. Younis and A. Moreira, "Interferometric Synthetic Aperture Radar (SAR) Missions Employing Formation Flying," in Proceedings of the IEEE, vol. 98, no. 5, pp. 816-843, May 2010, doi: 10.1109/JPROC.2009.2038948.

[11] R. Bahnemann et al., "Under the sand: Navigation and localization of a micro aerial vehicle for landmine detection with ground-penetrating synthetic aperture radar," Field Robotics, 2021.

[12] M. Villano et al., "Potential of Multi-Static SAR Systems for Earth Monitoring and Their Demonstration Using Swarms of Drones," IGARSS 2023 - 2023 IEEE International Geoscience and Remote Sensing Symposium, Pasadena, CA, USA, July 2023.

[13] A. Grathwohl et al., "Taking a Look Beneath the Surface: Multicopter UAV-Based Ground-Penetrating Imaging Radars," in IEEE Microwave Magazine, vol. 23, no. 10, pp. 32-46, Oct. 2022, doi: 10.1109/MMM.2022.3188126.

[14] Y. Á. López, M. García-Fernández, G. Álvarez-Narciandi and F. L. -H. Andrés, "Unmanned Aerial Vehicle-Based Ground-Penetrating Radar Systems: A review," in IEEE Geoscience and Remote Sensing Magazine, vol. 10, no. 2, pp. 66-86, June 2022, doi: 10.1109/MGRS.2022.3160664.

[15] S. Angelliaume, N. Castet and X. Dupuis, "SAR-Light: the new ONERA SAR sensor onboard UAV," EUSAR 2022; 14th European Conference on Synthetic Aperture Radar, Leipzig, Germany, 2022, pp. 1-4.

[16] S. -Y. Jeon et al., "Uav-Borne Bistatic Sar and Insar Experiments in Support of STV and SDC Target Observables," 2023 IEEE International Geoscience and Remote Sensing Symposium, Pasadena, CA, USA, 2023, pp. 1906-1909, doi: 10.1109/IGARSS52108.2023.10282077.

[17] R. Burr, M. Schartel, A. Grathwohl, W. Mayer, T. Walter, and C. Waldschmidt, "UAV-Borne FMCW InSAR for Focusing Buried Objects," *IEEE Geoscience and Remote Sensing Letters*, vol. 19, pp. 1–5, 2022, doi: 10.1109/lgrs.2021.3094165.

[18] S. Kim et al., "Multichannel W-Band SAR System on a Multirotor UAV Platform With Real-Time Data Transmission Capabilities," in IEEE Access, vol. 8, pp. 144413-144431, 2020, doi: 10.1109/ACCESS.2020.3014700.

[19] L. Moreira et al., "Drone-Borne P-band Single-Pass InSAR," 2020 IEEE Radar Conference (RadarConf20), Florence, Italy, 2020, pp. 1-6, doi: 10.1109/RadarConf2043947.2020.9266502.

[20] D. A. Yocky, and R. D. West, "*Unmanned Aerial Vehicle Synthetic Aperture Radar for Surface Change Monitoring",* No. SAND2022-12261. Sandia National Lab.(SNL-NM), Albuquerque, NM (United States), 2022.

[21] O. Frey and C. L. Werner, "UAV-borne repeat-pass SAR interferometry and SAR tomography with a compact L-band SAR system," EUSAR 2021; 13th European Conference on Synthetic Aperture Radar, online, 2021, pp. 1-4.

[22] M. Lort, A. Aguasca, C. López-Martínez and T. M. Marín, "Initial Evaluation of SAR Capabilities in UAV Multicopter Platforms," in IEEE Journal of Selected Topics in Applied Earth Observations and Remote Sensing, vol. 11, no. 1, pp. 127-140, Jan. 2018, doi: 10.1109/JSTARS.2017.2752418.

[23] G. Ruiz-Carregal et al., "Single and Repeat-Pass Interfeormetry Using the Ku-Band SAR-Drone System," IEEE 2024 International Geoscience and Remote Sensing Symposium, Athens, Greece 2024.

[24] Y. Wang et al., "First Demonstration of Single-Pass Distributed SAR Tomographic Imaging With a P-Band UAV SAR Prototype," in IEEE Transactions on Geoscience and Remote Sensing, vol. 60, pp. 1-18, 2022, Art no. 5238618, doi: 10.1109/TGRS.2022.3221859.

[25] M.-A. Lahmeri, et al., "UAV Formation Optimization for Communication-Assisted InSAR Sensing," ICC 2024 - IEEE International Conference on Communications, Denver, CO, USA, 2024, pp. 3913-3918, doi: 10.1109/ICC51166.2024.10622647.

[26] V. Mustieles-Perez, S. Kim, G. Krieger and M. Villano, "New Insights Into Wideband Synthetic Aperture Radar Interferometry," in IEEE Geoscience and Remote Sensing Letters, vol. 21, pp. 1-5, 2024, Art no. 4016205, doi: 10.1109/LGRS.2024.3453413.

[27] M. Pinheiro, A. Reigber, and A. Moreira, "Large-baseline InSAR for precise topographic mapping: A framework for TanDEM-X large-baseline data," in Advances in Radio Science, 2017.

[28] M. Pinheiro et al., "Generation of Highly Accurate DEMs Over Flat Areas by Means of Dual-Frequency and Dual-Baseline Airborne SAR Interferometry," in IEEE Trans. Geosci. Remote Sens., vol. 56, no. 8, pp. 4361-4390, Aug. 2018.

[29] F. T. Ulaby and M. C. Dobson, Handbook of Radar Scattering Statistics for Terrain. Norwood, MA, USA: Artech House, 1989.

[30] Y. Zeng, J. Xu and R. Zhang, "Energy Minimization for Wireless Communication With Rotary-Wing UAV," in IEEE Transactions on Wireless Communications, vol. 18, no. 4, pp. 2329-2345, April 2019, doi: 10.1109/TWC.2019.2902559.

[31] P. Prats-Iraola, “Airborne Differential SAR Interferometry,” Ph.D. dissertation, Universitat Politecnica de Catalunya, Barcelona, Spain, 2005.

[32] A. Meta, “Signal Processing of FMCW Synthetic Aperture Radar,” Ph.D. dissertation, TU Delft, Delft, The Netherlands, 2006.

[33] L. M. H. Ulander, "Impulse Response Function for Ultra-wideband SAR," EUSAR 2014; 10th European Conference on Synthetic Aperture Radar, Berlin, Germany, 2014, pp. 1-4.

[34] R. Goodman, S. Tummala and W. Carrara, "Issues in ultra-wideband, widebeam SAR image formation," Proceedings International Radar Conference, Alexandria, VA, USA, 1995, pp. 479-485, doi: 10.1109/RADAR.1995.522595.

[35] N. Yague-Martinez, M. Eineder, R. Brcic, H. Breit and T. Fritz, "TanDEM-X Mission: SAR Image Coregistration Aspects," 8th European Conference on Synthetic Aperture Radar, Aachen, Germany, 2010, pp. 1-4.

[36] R. Scheiber and A. Moreira, "Coregistration of interferometric SAR images using spectral diversity," in IEEE Transactions on Geoscience and Remote Sensing, vol. 38, no. 5, pp. 2179-2191, Sept. 2000, doi: 10.1109/36.868876.

[37] A. Reigber, "Range dependent spectral filtering to minimize the baseline decorrelation in airborne SAR interferometry," IEEE 1999 International Geoscience and Remote Sensing Symposium. IGARSS'99 (Cat. No.99CH36293), Hamburg, Germany, 1999, pp. 1721-1723 vol.3, doi: 10.1109/IGARSS.1999.772073.

[38] A. Reigber, P. Prats and J. J. Mallorqui, "Refined estimation of time-varying baseline errors in airborne SAR interferometry," in IEEE Geoscience and Remote Sensing Letters, vol. 3, no. 1, pp. 145-149, Jan. 2006, doi: 10.1109/LGRS.2005.860482.

[39] D. R. Stevens, I. G. Cumming and A. L. Gray, "Options for airborne interferometric SAR motion compensation," in IEEE Transactions on Geoscience and Remote Sensing, vol. 33, no. 2, pp. 409-420, March 1995, doi: 10.1109/TGRS.1995.8746022.

[40] A. Gruber, B. Wessel, M. Martone and A. Roth, "The TanDEM-X DEM Mosaicking: Fusion of Multiple Acquisitions Using InSAR Quality Parameters," in IEEE Journal of Selected Topics in Applied Earth Observations and Remote Sensing, vol. 9, no. 3, pp. 1047-1057, March 2016, doi: 10.1109/JSTARS.2015.2421879.

[41] D. Just and R. Bamler, “Phase statistics of interferograms with applications to synthetic aperture radar,” Appl. Opt., vol. 33, no. 20, pp. 4361– 4368, Jul. 1994.

[42] M. T. Hallikainen et al., "Microwave Dielectric Behavior of Wet Soil-Part 1: Empirical Models and Experimental Observations," *in IEEE Trans. Geosci. Remote Sens., vol. GE-23, no.* 1, pp. 25-34, Jan. 1985.

[43] R. Burr, M. Schartel, W. Mayer, T. Walter and C. Waldschmidt, "Lightweight Broadband Antennas for UAV based GPR Sensors," 2018 15th European Radar Conference (EuRAD), Madrid, Spain, 2018, pp. 245-248, doi: 10.23919/EuRAD.2018.8546552.

[44] R. Bamler, "Interferometric stereo radargrammetry: absolute height determination from ERS-ENVISAT interferograms," IGARSS 2000. IEEE 2000 International Geoscience and Remote Sensing Symposium, Honolulu, HI, USA, 2000, pp. 742-745 vol.2, doi: 10.1109/IGARSS.2000.861689.

[45] V. Mustieles-Perez et al., "Experimental Demonstration of UAV-Based Ultra-Wideband Multi-Baseline SAR Interferometry," EUSAR 2024; 15th European Conference on Synthetic Aperture Radar, Munich, Germany, 2024, pp. 1156-1161.

[46] R. Burr, M. Schartel, P. Schmidt, W. Mayer, T. Walter and C. Waldschmidt, "Design and Implementation of a FMCW GPR for UAV-based Mine Detection," 2018 IEEE MTT-S International Conference on Microwaves for Intelligent Mobility (ICMIM), Munich, Germany, 2018, pp. 1-4, doi: 10.1109/ICMIM.2018.8443526.